Kinetic Barrier Diagrams to Visualize and Engineer Molecular Nonequilibrium Systems

Emanuele Penocchio, Giulio Ragazzon

Spray Coating Experiments: Setups and Methodologies

The latest eBook from Advanced Optical Metrology. Download for free.

Spray Coating Experiments: Setups and Methodologies, is the third in our Thin Films eBook series. This publication provides an introduction to spray coating, three article digests from Wiley Online Library and the latest news about Evident's Image of the Year Award 2022.

Wiley in collaboration with Evident, are committed to bridging the gap between fundamental research and industrial applications in the field of optical metrology. We strive to do this by collecting and organizing existing information, making it more accessible and useful for researchers and practitioners alike.

EVIDENT
OLYMPUS

WILEY

NANO · MICRO small

www.small-journal.com

Kinetic Barrier Diagrams to Visualize and Engineer Molecular Nonequilibrium Systems

Emanuele Penocchio and Giulio Ragazzon**

Molecular nonequilibrium systems hold great promises for the nanotechnology of the future. Yet, their development is slowed by the absence of an informative representation. Indeed, while potential energy surfaces comprise in principle all the information, they hide the dynamic interplay of multiple reaction pathways underlying nonequilibrium systems, i.e., the degree of kinetic asymmetry. To offer an insightful visual representation of kinetic asymmetry, we extended an approach pertaining to catalytic networks, the energy span model, by focusing on system dynamics – rather than thermodynamics. Our approach encompasses both chemically and photochemically driven systems, ranging from unimolecular motors to simple self-assembly schemes. The obtained diagrams give immediate access to information needed to guide experiments, such as states' population, rate of machine operation, maximum work output, and effects of design changes. The proposed kinetic barrier diagrams offer a unifying graphical tool for disparate nonequilibrium phenomena.

1. Introduction

Representation shapes how we perceive the world, thus, how we think about it. It is pervasive in our society, having a profound impact on our lives. Science as well heavily relies on the visualization of systems at study. Indeed, many scientific breakthroughs are tightly associated with representation, as exemplified by the discovery of the periodic table[1,2] and the effectiveness of hand-drawings to describe complex phenomena such as reactions' mechanisms.[3] The concept of potential energy surfaces also profoundly impacted the understanding of chemical reactions. First proposed in 1915, this concept underlies most areas of chemistry, including electron transfer reactions, transition state (TS) theory, supramolecular chemistry, and the development of molecular machines.[4,5] Yet, some limitations of the potential energy surface representation of chemical systems start to emerge, e.g. when considering reaction networks that include both first- and second-order rate constants, as recognized by Knowles et al..[6,7] Issues arise also at the forefront of supramolecular chemistry and molecular machines when dealing with nonequilibrium systems, which hold great promises for future nanotechnology development.[8–10] The reason is that autonomous molecular machines are accurately described by periodic multidimensional potential energy surfaces, that include multiple pathways, and appear even tilted while the machine operates autonomously (**Figure 1**a).[11,12] Multidimensional representations are more difficult to use than simple 1D representations. Indeed, their use is rather limited among experimentalists. Similar representations apply to self-assembling systems that can exploit an energy source to assemble high-energy structures. Dissipative self-assembly is a lively area of supramolecular chemistry, where the fundamental principles are even less explored. In this context, a common representation relies on extremely simplified potential energy profiles lacking specific details (Figure 1b).[13–15]

In autonomous molecular machines and nonequilibrium self-assembly, systems' operation can be represented with chemical reaction networks including multiple catalytic paths (**Figure 2**).[16,17] Rationalizing the mutual influence between the available paths can be hard, and the effects of changing reaction rates are frequently not trivial, also because accelerating the rate of one reaction will always result in the acceleration of its microscopic reverse if the free energy change remains the same.[18] For experimentalists working in the area, it would be beneficial having a simple representation of nonequilibrium systems, informing on how to optimize machine ability to perform work or the assembly of a nonequilibrium species (Figure 1c). At present, addressing these questions requires convoluted studies.[19–22]

E. Penocchio
Department of Physics and Materials Science
University of Luxembourg
Luxembourg L-1511, Luxembourg

E. Penocchio
Department of Chemistry
Northwestern University
Evanston, IL 60208, USA
E-mail: emanuele.penocchio@northwestern.edu

G. Ragazzon
University of Strasbourg
CNRS
Institut de Science et d'Ingégnierie Supramoléculaires (ISIS) UMR 7006
8 allée Gaspard Monge, Strasbourg F-67000, France
E-mail: ragazzon@unistra.fr

The ORCID identification number(s) for the author(s) of this article can be found under https://doi.org/10.1002/smll.202206188.

DOI: 10.1002/smll.202206188

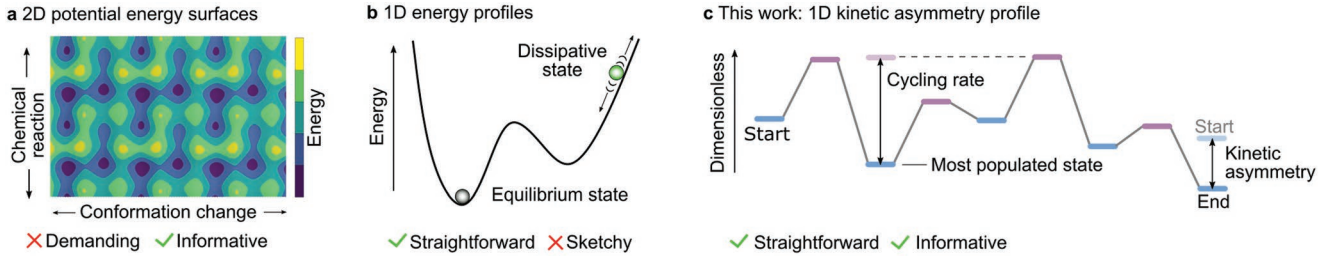

Figure 1. Different graphical representations are used to describe nonequilibrium systems. a) 2D equilibrium potential energy surface for a hypothetical molecular machine coupling conformation changes to chemical reactions, as a typical example of high-resolution representation, with continuous degrees of freedom and detailed free-energy landscape. The free-energy valley along which a force can possibly drive the system might be guessed, but there's no immediate clue about directionality (kinetic asymmetry). Accurate data on systems' energetics are required. b) Generic 1D profile is a typical example of abstract representation. The out-of-equilibrium nature of the system is made clear, but no concrete information is conveyed. No data about the system are required. c) A graphical and discrete representation of systems' kinetics, able to visually convey relevant dynamic features, is proposed in this work as kinetic barrier diagram. Information about directionality, order of magnitude of the cycling rate, most populated intermediate, and rate-limiting feature of experimental systems are embedded and can be deduced by following simple graphical rules explained in the main text and in the interactive tutorial (see Supporting Information). Data on systems' kinetics are required.

Most artificial molecular motors combine two orthogonal reactions, which result in square reaction schemes -also known as bipartite networks.[23,24] In these cases, one reaction is associated with mechanical motion (e.g., rotation) and the other is associated with an energy source (e.g., photoisomerization).[25–28] Therefore, square schemes are ideal to discuss the properties of artificial molecular motors, as they include the most important features of nonequilibrium networks while remaining simple.

To introduce our approach, in the following we consider a network that models a hypothetical chemically driven autonomous rotor, tightly related to a recently reported motor rotating about a covalent single bond (Figure 2a).[29,30] The rotor M can interconvert between two different forms by performing half a rotation (reaction 4 in Figure 2a). This reaction is associated with a mechanical movement, affording M'. Reactions 1 and 3 are instead associated with the interactions with a chemical fuel[31] (F) and its conversion into a waste product (W). The binding of F to the motor (reactions 1F and 3F in Figure 2a) converts it into "bound" forms M* or M'*. Under the same conditions, F can be released as W (reaction 1 and 3 W in Figure 2a) reverting the system to the free forms M and M'. In many cases, the conversion of F into W is a highly exergonic reaction, i.e., "irreversible" from the experimental point of view. Examples are phosphate hydrolysis, carbodiimide hydration, or decarboxylation reaction.[30,32,33] However, to respect microscopic reversibility[18] and ensure a correct analysis, all reactions are formally described as reversible, even when practically "irreversible". The last reaction to be introduced is the mechanical motion interconverting the bound states, M* and M'* (reaction 2 in Figure 2a). If rotation around the aryl-aryl bond occurs in the same direction (e.g., clockwise) in reactions 2 and 4, the sequence of reactions 1→2→3→4 affords the unidirectional rotation of one aryl unit with respect to the other. Under equilibrium conditions, this sequence occurs with the same likelihood of the opposite: 4→3→2→1, canceling any directionality.

The energy required for directionality to appear is provided by the conversion of high energy F into W. To study such nonequilibrium conditions, systems are analyzed under a constant turnover of F into W by fixing – chemostatting – the concentrations of F and W at values that are not compatible with equilibrium for the F ⇋ W reaction. Thus, the system will evolve toward a steady state in which F is continuously converted into W.[34] The sequence of reactions used to convert F into W becomes crucial in determining the observed behavior. The square scheme offers four distinct pathways for converting F into W mediated by the machine (Figure 2b), but only paths III and IV are coupled with mechanical movements. Path III corresponds to reactions F + M ⇋ M* ⇋ M'* ⇋ M' + W, resulting in the overall reaction F + M ⇋ M'+ W. Thus, the con-

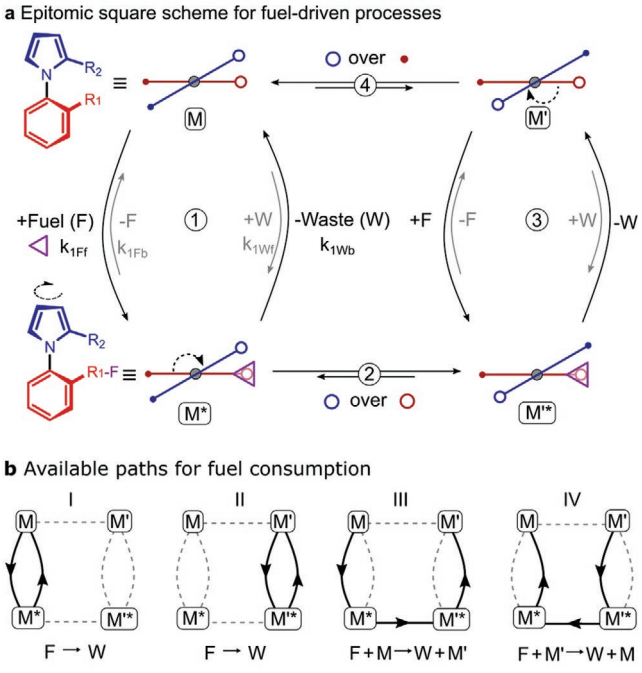

Figure 2. Square reaction network for a fuel-driven process. a) Epitomic reaction network associated with the operation of a four-state chemically driven rotor, including notation associated with Step 1. The network has been described in ref. [29] and is tightly related to the rotor described in ref. [30]. b) Indication of the multiple paths available for F to W conversion catalyzed by the rotor.

version of F to W affords at the same time the conversion of M to M'. Path IV promotes the opposite reaction according to reactions F + M' ⇋ M'* ⇋ M* ⇋ M + W, which couples F to W conversion with M' transformation into M. Under continuous F turnover, all pathways participate in converting F into W. It is only a matter of kinetics which one will prevail. Key to the system behavior is therefore the kinetic competition between oppositely coupled paths III and IV. When one of these paths prevails over the other, the system can be described as kinetically asymmetric, with two important consequences. The first effect is that a cyclic chemical current emerges, e.g., if path III prevails a counterclockwise current arises, with M' is constantly produced via reactions 1→2→3 while simultaneously consumed via reaction 4. The second effect is that reactions 2 and 4, which do not involve chemostatted species F or W, can be kept out-of-equilibrium. These two effects are important because they underlie both the operation of autonomous motors and endergonic self-assembly. Indeed, when the catalytic cycle coincides with the operation of a molecular machine, maximizing the current accelerates the operation. On the other hand, if the target is the assembly of a high-energy species, the system should be optimized to drive the concentrations of such species away from the corresponding equilibrium. On top of this, the maximum amount of energy that can be stored in such a high-energy assembly, as well as the maximum amount of work that a molecular machine can perform, are related to the extent of kinetic asymmetry, which is the essential operating principle of molecular machines that operate under constant environmental conditions and can be quantified by the ratcheting constant K_r.[16,35–38]

Here, we propose a simple strategy to represent molecular systems displaying kinetic asymmetry and operating under constant environmental conditions, leading to a dimensionless diagram denoted "kinetic barrier diagram," in line with the terminology used by Knowles to describe the kinetics of enzymatic activity.[6,7] Kinetic barrier diagrams visually map system dynamics, giving immediate access to the features normally requiring optimization in real systems.

2. Results

Inspired by the close relation of chemically driven nonequilibrium systems with catalytic processes, we considered if the tools developed in the context of chemical catalysis could be fruitfully employed for the rationalization of artificial nonequilibrium systems.[39–42] In particular, we focus on the energy span model, useful to rationalize catalytic cycles.[41,43–45] This model shows that the rate of catalytic cycles is determined by the whole energy span explored during a cycle. To illustrate this idea, we consider the potential energy profile associated with a catalytic cycle involving path IV, identified as cycle IV (**Figure 3**a). After one cycle, the motor (i.e., catalyst) returns to the initial state, while the system energy has decreased, accounting for the conversion of F into W, $\Delta G_{F \rightarrow W}$. The turnover frequency (TOF) of this catalytic cycle is related to its energy span, as the latter is the energy difference between the TS and the intermediate that mostly contribute to determine the TOF, which are respectively identified as TOF-determining TS and TOF-determining

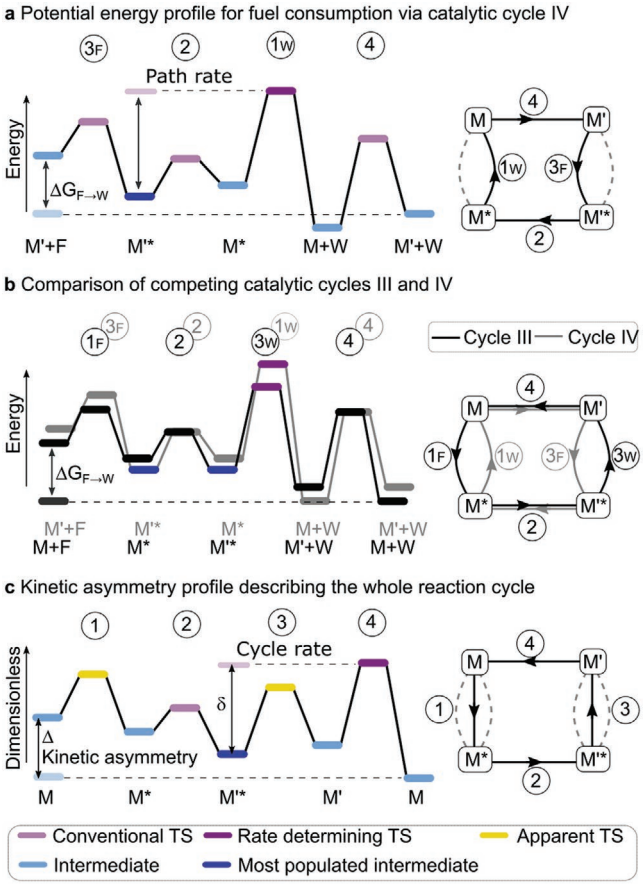

Figure 3. Diagrams representing square scheme networks. a) Potential energy profile associated with F to W conversion via catalytic cycle IV. b) Comparison of potential energy profiles for cycles III and IV. c) Kinetic barrier diagram is constructed as explained in Section 2.1.

intermediate. To facilitate readers and with no loss of generality, in this manuscript, the TOF-determining TS coincides with the highest energy TS, and the TOF-determining intermediate coincides with the most stable intermediate appearing before the TOF-determining TS.[43] Thus, the energy span reports quantitatively on the rate at which the considered catalytic cycle operates and is visually immediate to identify.[43] Therefore, in the illustrated example, to accelerate the TOF of the catalytic cycle associated with path IV, two effective strategies would be to stabilize the TS of reaction 1 W or destabilize the intermediate M'*. Importantly, the TOF-determining intermediate corresponds to the most populated state, providing direct access to state populations under stationary nonequilibrium conditions.

The first approach to apply the energy span model to catalysis-driven motors is to represent the competing catalytic cycles associated with coupled reaction paths III and IV (Figure 3b).[44] If the two cycles have the same TOF, the system is kinetically symmetric (K_r = 1). In the pictured scenario, the two cycles share the same TOF-determining intermediate, M'*. Therefore, the TOFs are largely dictated by the energies of the less stable TSs, which can be different for the two cycles because they are associated with different reactions (3 and 1 W). One possibility

leading to kinetic asymmetry emergence is that the energies of TSs are such that the release of W is favored in the M'* state, i.e., the TS for reaction 3 W is lower than TS for reaction 1 W.[37,38] In such a case, cycle III will be kinetically preferred, resulting in the coupled conversion of M into M'. Thus, TS energies of competing cycles are what should be "asymmetric" for a current to arise. On the contrary, comparing rate constants is often not informative, because they reflect the energy difference between neighbor states. Therefore, even in a symmetric system, rate constants might all have different values.

Despite representing competing cycles' potential energy profiles offers some insight, most system features remain hidden "at first glance". Thus, with a direct application of the energy span model it remains complicated to understand immediately if the motor will cycle, in which direction, how its performance can be improved, and which state will be the most populated one. To obtain a straightforward and informative representation, we detach from energetics and focus solely on the system's dynamics. To do so, we change how steps comprising multiple reactions are described – here Steps 1 and 3. In these steps, the starting and end state, e.g., M and M* for step 1, are connected via two different reactions involving either F or W. In such cases, the two conventional rate constants are replaced by one effective rate constant, which reflects the overall rate at which the states interconvert, regardless of the reaction path taken. Therefore, effective rates report on the intermediate's dynamic kinetic stability.[46] Mathematically, the effective rate constant is the sum of the two individual rate constants, multiplied by chemostatted concentrations [F] and [W] in the case of second-order constants (e.g., $k_{1f} = [F]\, k_{1Ff} + [W]\, k_{1Wf}$ according to the notation in Figure 2a). These effective rate constants are used to calculate the dimensionless height of a corresponding effective TS via an Eyring-like equation, thus in the present example, the dimensionless quantity $-\ln(k_{1f}h/k_BT)$ gives the height of the effective barrier to go from M to M*, with h, k_B, and T the Plank constant, the Boltzmann constant, and the temperature, respectively. By doing this, the resulting effective TS reflects the combined kinetic stability of M, taking into account both reaction paths leading to M*. As detailed in Section 2.1, calculating the dimensionless height for every step of the square scheme uniquely defines the kinetic barrier diagram reported in Figure 3c. The diagram reflects the kinetic features of the system, while thermodynamic information is lost. For an arbitrary N-state network that can be represented using a single cyclic path, the corresponding kinetic barrier diagram is characterized by a set of N effective transition states with heights $\{T_1, ..., T_N\}$, and a set of N+1 intermediates with heights $\{I^0_N, I_1, ..., I_N\}$, with $I^0_N = 0$ an arbitrary starting point. The advantage of kinetic barrier diagrams over conventional potential energy profiles is making all the most important information accessible at a glance. To start with, the height of the final state appears lower than the height of the initial state by $\Delta := I_M - I^0_M = -\ln(K_r)$, reporting on kinetic asymmetry, thus directionality ($\Delta = 0$ for a kinetically symmetric system, $\Delta < 0$ if clockwise cycling is favored, Section I-A, Supporting Information). Kinetic asymmetry is immediately visualized as a tilted diagram, characteristic of nonequilibrium systems.[47] The tilt is a purely kinetic phenomenon, with Δ representing an upper bound for the work (in dimensionless units of RT) that the machine could perform against a load via the conformational rearrangement steps 2 and 4 (Section I-D, Supporting Information).

Importantly, the proposed approach allows applying the tools of the energy span model in a mathematically rigorous way.[41] Indeed, the motor's TOF can be exactly expressed in terms of the kinetic barrier diagram as (Section I, Supporting Information):

$$\mathrm{TOF} = \frac{k_B T}{h}\left(e^{-\Delta} - 1\right) \Big/ \sum_{i = M, M*, M'*, M'} \; \sum_{j = 1,2,3,4} e^{T_j - I_i - \Delta_{i,j}} \tag{1}$$

with

$$\Delta_{i,j} = \begin{cases} \Delta := I_M - I^0_M, & \text{if } T_j \text{ follows } I_i \text{ in the profile (as always herein)} \\ 0, & \text{if } T_j \text{ precedes } I_i \text{ in the profile} \end{cases} \tag{2}$$

Crucially, due to the exponential terms in Equation (1), the order of magnitude of the denominator will be typically dominated by the term with the largest value of $T_j\text{-}I_i\text{-}\Delta_{i,j}$, or by the n largest ones in case of degeneracy. Furthermore, when kinetic asymmetry is present ($\Delta < 0$, which is the case of interest here) the –1 term at the numerator can be neglected (as a rule of thumb, the approximation works fine for $\Delta < -2$). As a consequence, the expression of the TOF in Equation (1) can be approximated to

$$\mathrm{TOF} \approx \frac{k_B T}{nh} e^{-\delta} \tag{3}$$

where n is the number of degenerate terms discussed above, and with

$$\delta = \begin{cases} T_{TDT} - I_{TDI}, & \text{if } T_{TDT} \text{ follows } I_{TDI} \text{ in the profile (as always herein)} \\ T_{TDT} - I_{TDI} + \Delta, & \text{if } T_{TDT} \text{ precedes } I_{TDI} \text{ in the profile} \end{cases} \tag{4}$$

where T_{TDT} denotes the height of the TOF-determining effective TS and I_{TDI} the height of the TOF-determining intermediate, i.e., the couple of T and I maximizing δ (Section I-B, Supporting Information).[43] Equation (3) is a key result of our treatment. It shows that a single parameter (δ), visually deducible from the kinetic barrier diagram, quantitatively reports on the TOF of a kinetically asymmetric network. In the same way, as for the following examples, the conditions under which Equation (3) proves a good approximation are met by the majority of kinetically asymmetric systems developed to date. In general, this condition can be easily checked by inspecting the diagram and considering if $|\Delta| > 2$, the above-mentioned rule of thumb. Furthermore, kinetic barrier diagrams can be used even when Equation (3) is not valid. In those cases, the TOF should be computed with Equation (1), therefore losing the graphical intuition provided by Equation (3). However, the graphical information on directionality and maximum work output given by Δ are preserved, and one can still gain intuition on the kinetic features of the system.

The span δ also identifies the intermediate and TS regulating the current, e.g., in Figure 3c TS 4 and intermediate state

M'*, giving immediate access to strategies for motor optimization. With the target of maximizing machine rate, the largest effects are expected by stabilizing TS 4 (lowering T_4) or destabilizing M'* (raising $I_{M'*}$). Instead, changing the stability of TS 3 or M* would only marginally affect the overall rate. This consideration illustrates that intermediates' stabilities play a major role in determining the rate of cycling: a too stable intermediate acts as a sink, and a very unstable one hampers efficient cycling, despite not altering kinetic asymmetry. Kinetic barrier diagrams give also information on intermediates' population. Indeed, the TOF-determining intermediate is the most populated state under nonequilibrium conditions (Section I-C, Supporting Information). This information is particularly useful when the target is to accumulate a high-energy species. Also, when considering how to monitor the system, it enables anticipating which concentration changes will occur upon varying the experimental conditions. Insights remain fully coherent with related theoretical results, e.g., varying only the equilibrium constant for Steps 2 and 4 does not influence the directionality of the system (Δ), which confirms being a purely kinetic phenomenon.[12,37,38,48] To illustrate the insight offered by this approach in different contexts, we have constructed the kinetic barrier diagrams for three significant systems reported in the literature: a chemically driven motor, a light-driven motor, and the driven self-assembly of dimers.[33,37,49] Moreover, to help the reader familiarize with kinetic barrier diagrams, we provide an interactive tutorial in form of a Jupyter Notebook as supplementary material, which can be used to explore the features of kinetic barrier diagrams. As an example, it can be used to show that by altering just TS energies it is possible to dictate the net tilt of the surface in either direction.

2.1. How to Construct a Kinetic Barrier Diagram

Here, we detail how to construct the kinetic barrier diagram for the square system depicted in Figure 3c, operating at chemostatted concentration of Fuel and Waste.

1) Define the effective rate constants. For reactions that involve F or W, multiply the associated rate constant for the fixed concentration of F or W. For steps that can occur via two different pathways, sum the two rate constants that are associated with transitions from one state to the other. As an example, $k_{1f} = [F]\ k_{1Ff} + [W]\ k_{1Wf}$ and $k_{1b} = k_{1Fb} + k_{1Wb}$, according to the notation in Figure 2a.
2) Calculate the effective barriers. Use the measured and calculated rate constants in an Eyring-like equation, e.g. for k_{1f}: height = $-\ln (k_{1f}h/\ k_BT)$ and for k_{1b}: height = $-\ln (k_{1b}h/\ k_BT)$
3) Construct the diagram.
   3a) Define a starting intermediate, e.g. M, which will have height $I^0_M = 0$ by convention.
   3b) Draw the effective transition state encountered in the forward direction by summing the dimensionless height associated with the considered transition, e.g. TS1 having height $T_{S1} = I^0_M - \ln (k_{1f}h/\ k_BT)$. Then, place the following intermediate by subtracting the height associated to the backward transition, e.g. M* having height $I_{M*} = T_{S1} + \ln (k_{1b}h/\ k_BT)$.
   3c) Repeat 3b to place the following transition state and intermediate, until the starting state, e.g. I_M, is positioned, thus completing the cycle.

2.2. Kinetic Barrier Diagrams for Chemically Driven Motors

The first system that we describe using kinetic barrier diagrams is the first autonomous chemically driven motor, in which the consumption of a high-energy F promotes directional rotation in a catenane (**Figure 4**a).[33] The motor comprises a circular track with two binding sites for a macrocycle. The latter can shuttle between the two stations, but this movement can be prevented by fluorenylmethoxycarbonyl barriers, which are continuously added and removed via the consumption of F. Directionality emerges under continuous F consumption because the barrier-forming reaction is slower when the macrocycle is proximal to the barrier-formation site, most likely due to steric crowding effects. This effect is indicated as kinetic gating and is the molecular origin of kinetic asymmetry for this system.[50] Instead, the rate constants of all the other reactions are unaffected by the location of the macrocycle. Thus, on average, shuttling in the clockwise direction by overcoming the proximal barrier-forming site is more likely than shuttling in the counterclockwise direction by overcoming the distal barrier-forming site. To perform a directional cycle, a motor needs to invert which barrier is in place (vertical reactions in Figure 4a). Under experimental conditions, this process occurs via a state having two barriers simultaneously present, affording the pictured six-state scheme.

The behavior of the motor is anticipated by the corresponding kinetic barrier diagram drawn in Figure 4b. The presence of kinetic asymmetry is immediately evident by a negative difference (Δ = −3) between the heights of the final and starting states of one counterclockwise operation cycle, thus indicating the kinetic preference for this direction. In this context, Δ is an upper bound for the work (in dimensionless units of RT) that such motor could perform on the environment. The origin of kinetic asymmetry, kinetic gating, is visualized by the effective activation energies for Steps 1 and 3, which appear higher when the macrocycle is proximal to the barrier-formation site, e.g., TS-1^p lies higher than TS-3^d. Because of the high symmetry of the system, the six-state cycle has two identical halves, which result in two degenerate rate-determining TSs that determine the span of the kinetic barrier diagram. Already at the qualitative level, it is observed that the motor's TOF depends on the height of effective TSs. This insight is important because the TOF corresponds to the net frequency with which a single macrocycle rotates in the forward direction. According to Equation (3), a good estimate of the motor's TOF is given by $\text{TOF} \approx (k_BT/2\ h)\ e^{-\delta}$, where the factor 1/2 is required by the presence of the two degenerate TOF-determining states.[12] Remarkably, the predicted TOF (10^{-6} s^{-1}) corresponds with the one calculated by numerical simulations.[24]

Our graphical approach based on effective TS predicts the effect of design variations. For instance, one possible modification is altering stations' stability. The kinetic barrier diagram obtained upon stabilizing the yellow – deuterated – station is shown in Figure 4c. Breaking stations' degeneracy does not

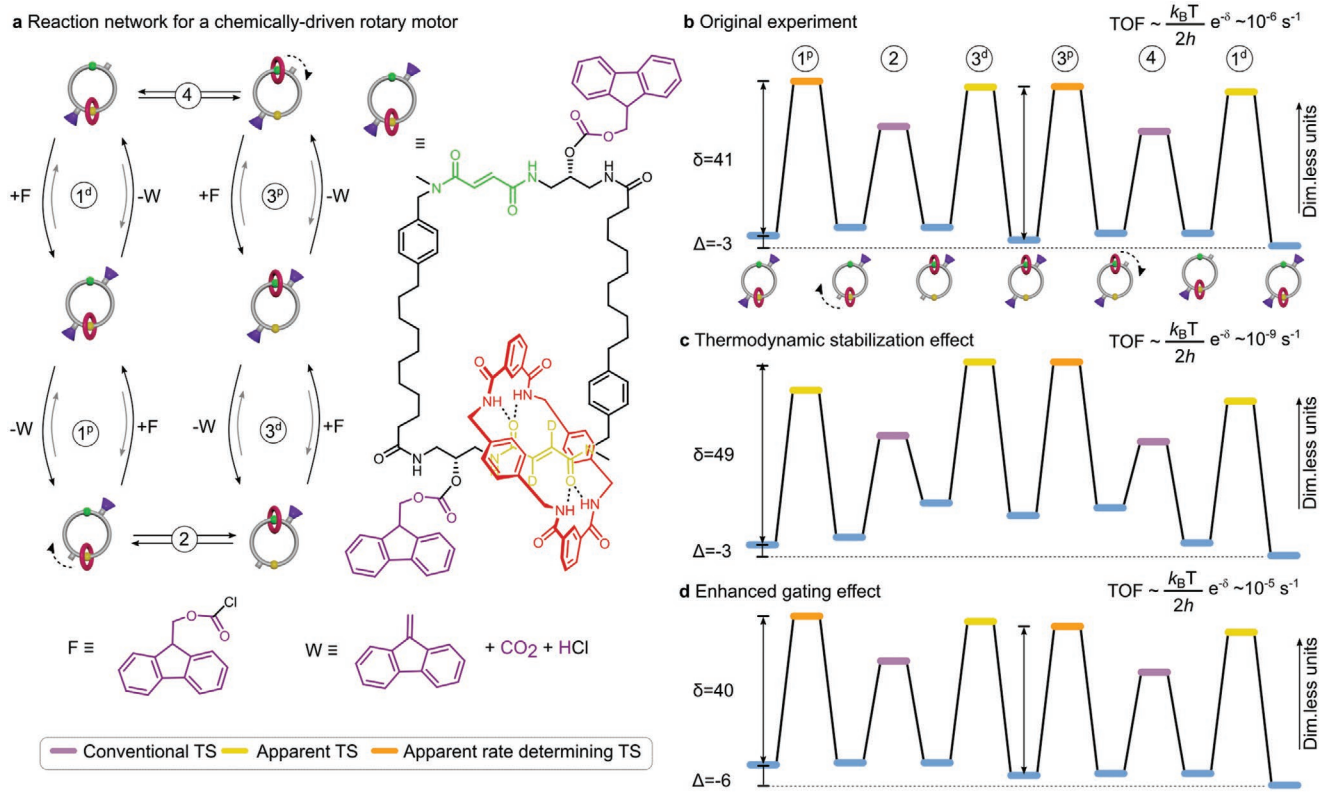

Figure 4. Insights on an artificial fuel-driven rotary motor. a) Reaction network and molecular structures of catenane rotor.[33] b–d) Kinetic barrier diagrams for various versions of the motor (Table S1, Supporting Information for parameters).[24] b) Original experiment. c) Motor having recognition sites with different affinity for the macrocycle. d) Doubly kinetically-gated motor, obtained by introducing a catalytic effect for barrier removal when the macrocycle is proximal to the reaction site.

alter kinetic asymmetry, thus the directionality, but significantly slows down the motor by increasing the value of δ. The second hypothetical variation explored is adding a kinetic gating effect at the level of barrier removal reactions too, i.e., making the macrocycle able to catalyze barrier removal when proximal to the reaction site.[51] As seen from Figure 4d, enhancing the kinetic gating increases the kinetic asymmetry of the cycle ($\Delta = -6$) and reduces the span ($\delta = 40$) at the same time, leading to an increase in the motor operation rate. In both cases, visual predictions are in full agreement with conventional numerical simulations.[24] In this context, we envision that our approach can be helpful in guiding both new experiments and non-equilibrium molecular dynamics simulations searching for optimal working conditions of this and other chemically driven motors.[52]

2.3. Kinetic Barrier Diagrams for Light-Driven Machines

Focusing on systems' dynamics allows employing kinetic barrier diagrams to describe systems that operate according to different thermodynamic principles. To demonstrate this versatility, we apply the proposed diagrams to light-driven motors based on photoswitches, which are widely employed modules to activate light-driven systems.[53–55] In particular, we consider a second-generation light-driven rotary motor, which is capable of MHz rotation – under appropriate irradiation conditions.[49,53] The motor in the study can be described by a square scheme resembling the one depicted in Figure 2a, but having steps 1 and 3 which are now light-induced photoisomerization reactions (**Figure 5**a). Under appropriate optical conditions, the rate of isomerization can be described by first-order rate constants (Equation S20, Supporting Information). The ratio between forward and backward isomerization rates reflects the composition at the photostationary state, which is an experimentally accessible quantity. The photochemical rate constants can be used in an Eyring-like equation to obtain an effective TS for photoisomerization. The height of this barrier has solely dynamic significance, with no thermodynamic meaning. However, it allows for drawing meaningful kinetic barrier diagrams for optically-driven systems (Figure 5b).

The motor has a very large kinetic asymmetry, arising from the highly exergonic thermal steps. The relevance of thermal steps is a direct consequence of the different principles underlying light-driven systems and chemically driven ones.[56,57] Indeed, systems based on photoswitches allow the simultaneous occurrence of information and energy ratchet effects, which is prevented in chemically driven systems.[21] When analyzing the rotation rate, the less stable TS are the two effective photochemical states characterized by a practically degenerate span. Therefore, the rate of isomerization, thus illumination conditions, dictates motor operation rate

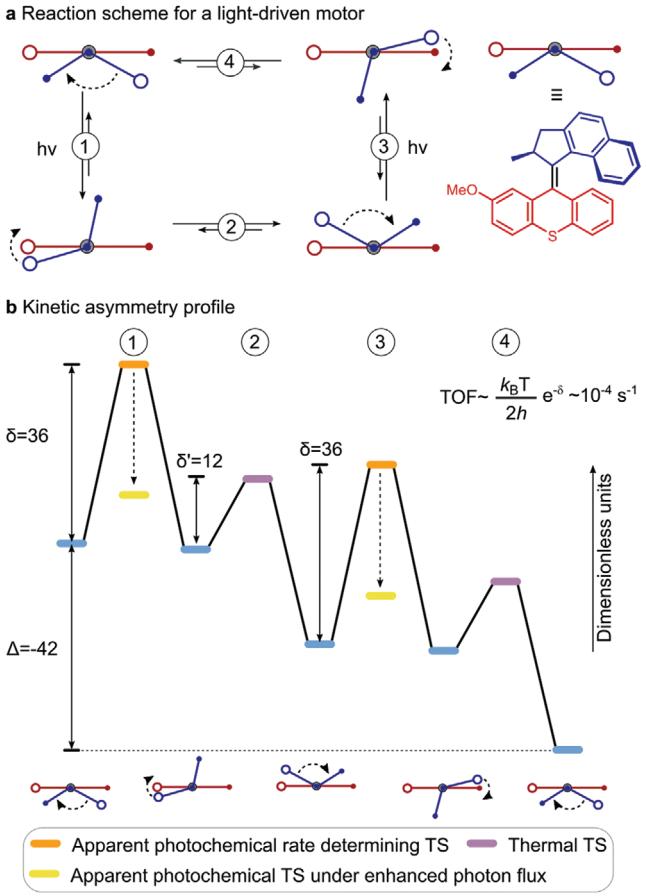

Figure 5. Insights on a light-driven rotary motor. a) Reaction network and molecular structure of light-driven rotary motor (Table S2, Supporting Information for parameters).[48] b) Associated kinetic barrier diagram. The effect of increasing the photon flux is indicated using dashed arrows.

at the bulk level. To construct the discussed kinetic barrier diagrams, we have considered the photon flux of an experimentally employed mercury lamp (Table S2, Supporting Information).[55] Under such an illumination, the span ($\delta = 36$) anticipates a 10^{-4} Hz rotation frequency. Since the timescale of the thermal steps is in the order of MHz, to approach the maximum possible speed of rotation, the simplest approach is to increase the photon flux. This operation is reflected in the kinetic barrier diagrams by a decrease in the height of both effective photochemical TSs. In contrast, the height of all the intermediates – dictated by the photostationary state composition – remains unchanged as long as photostationary states remain unaltered. This analysis warns about the relevance of photochemical reaction rates, which involve ultrafast events but may have a rather slow speed at the ensemble level, dictated by the slow frequency at which photons are absorbed under conventional irradiation conditions. Indeed, a strong dependence of molecular machine performance on light intensity has recently been demonstrated for a light-driven molecular pump, suggesting a dominating role for photo-induced processes in several photoactive artificial systems.[58]

2.4. Kinetic Barrier Diagrams for Driven Self-Assembly

As a final example, we apply kinetic barrier diagrams in the context of driven self-assembly.[37,59] In this case, the target is to maximize the population of a high-energy species. Under nonequilibrium conditions, the most populated state coincides with the TOF-determining intermediate. Thus, to accumulate this species, the reaction affording the target state should be highly exergonic, and a kinetic barrier should prevent its disassembly. These requirements are indeed found in the nonequilibrium self-assembly of microtubules, in which the high-energy microtubule following an exergonic phosphate hydrolysis step remains kinetically trapped. To illustrate how kinetic barrier diagrams can guide the optimization of driven self-assembling systems, we focus on a minimalist model describing the fuel-driven self-assembly of dimers (**Figure 6**a), employed frequently to discuss this phenomenon.[16,22,37,38,60]

The scheme resembles the square scheme discussed in the previous sections, except that now self-assembling processes replace conformational changes (Figure 6a). In particular, a low-energy monomer (blue sphere) can self-assemble to give a high-energy dimer (reaction 4). To build a meaningful kinetic barrier diagram in the presence of these bimolecular steps, the steady-state concentrations of the monomer ([M]) and the bound monomer ([M*]) must be included in the effective kinetic constants defining the height of self-assembling TSs (e.g., $\Delta G_{eff2} = -\ln(k_{2f}[M^*]h/k_BT)$). Therefore, all TSs become effective (Section IV, Supporting Information). Crucially, obtaining kinetic barrier diagrams for these kinds of nonlinear schemes remains possible. One possibility is to postprocess numerical kinetic simulations and build the kinetic barrier diagram following the same procedure as in Section 2.1 using the steady state concentrations [M] and [M*] obtained from the simulations as additional parameters. Another possibility, equivalent and employed here, is to use a self-consistent algorithm, which requires no additional information besides the effective kinetic constants, thus extending the range of applicability of the energy span approach beyond linear systems (Section IV-A, Supporting Information).[44] Importantly, in this case, the expression of Δ using the effective rate constants $k_{jf,jb}$ is

$$\Delta = -\ln\frac{[M^*]k_{1f}k_{2f}k_{3f}k_{4f}}{[M]k_{1b}k_{2b}k_{3b}k_{4b}} \quad (5)$$

which incorporates a dependence on the concentration of monomers at steady state (SI equation S.26). Therefore, our analysis generalizes the expression of kinetic asymmetry in self-assembling systems[37] to account for concentration effects.

To illustrate the predictive power of our approach in relation to nonequilibrium self-assembly, we draw kinetic barrier diagrams for the present scheme on varying of [F] while keeping all the other parameters constant. In this context, the analysis focuses on the most populated state, which coincides with the TOF-determining intermediate. As expected, when [F] is such that $\Delta G_{F \to W} = 0$, the predicted steady-state is an equilibrium one. In the absence of kinetic asymmetry ($\Delta = 0$), the low-energy free monomer is the most populated intermediate (Figure 6b). As [F] increases, the system evolves into nonequilibrium steady states, with kinetic asymmetry visually

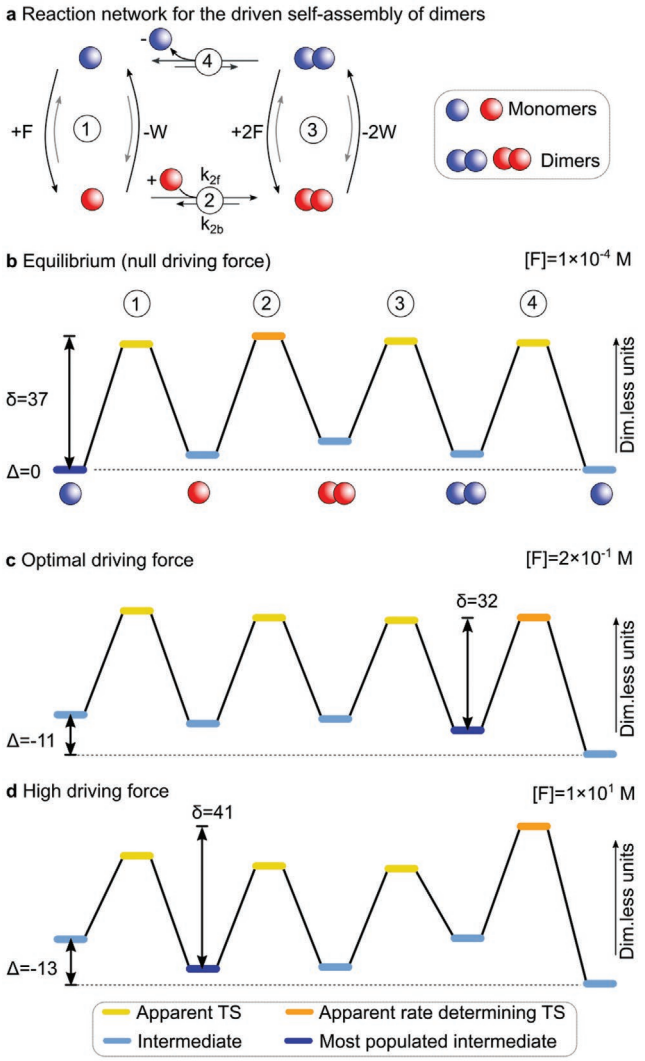

Figure 6. Insights on fuel-driven self-assembly of dimers. a) Reaction network as proposed in ref. [37]. b–d) Kinetic barrier diagrams for various values of [F] (Table S3, Supporting Information for parameters).[22] b) Equilibrium condition. c) The optimal condition for dimer accumulation. d) High [F] condition.

reported by values of $\Delta < 0$. When [F] approaches 200 mM, the dimer itself becomes the TOF-determining intermediate, the ideal condition for accumulating this high-energy species (Figure 6c). At high [F], the change in the shape of the kinetic barrier diagram predicts the steady-state distribution to become rich in bound monomer, which becomes the TOF-determining intermediate (Figure 6d). Again, predictions from kinetic barrier diagrams are perfectly aligned with more convoluted analyses, which recognized such a twofold behavior in the ability to accumulate dimers.[22,60] The fact that increasing the driving force is beneficial up to an optimal value of [F] and detrimental above it is a chemical example of a negative differential response to a driving force, a hallmark of far-from-equilibrium physical systems.[60] In the context of self-assembling systems, Δ is an upper bound to the energy stored in self-assembling steps. At the same time, it is not granted that increasing Δ will lead to an increase in the stored energy because these two quantities coincide only in the limit of fast F turnover.

3. Discussion and Conclusion

We have presented kinetic barrier diagrams as a visual means to anticipate the properties of molecular nonequilibrium systems at a glance. Focusing on systems' dynamics by introducing effective TS enables extending the energy span theory to nonequilibrium systems, shifting the attention from rate constants to a dimensionless diagram. As a result, a formally reliable framework becomes available to anticipate the directionality and speed of analyzed systems, already upon visualization of the diagram. The discussed examples illustrate systems that exploit different energy sources and require the optimization of different aspects, such as chemical current (machine operation rate) or accumulation of a species beyond its equilibrium population. The cost for having an immediately accessible diagram is that thermodynamic information is lost, and extreme care should be taken when retrieving thermodynamic information from kinetic barrier diagrams, which should be seen just as convenient illustrative representations.[6] Still, a specific connection can be retrieved: the upper limit for stored energy (coinciding with the maximum work output) is associated with kinetic asymmetry, thus Δ. Moreover, our work expanded the energy span theory to nonlinear systems, offering a generalized expression of kinetic asymmetry accounting for changes in the catalyst (e.g., monomers) concentration.

Our analysis shows that two readily visible parameters bear the information on motor directionality (Δ) and rate (δ). These are global properties that emerge when considering the whole diagram. Concretely, they allow for identifying the steps controlling system cycling rate and populations, two of the most relevant insights for the experimental observation and engineering of such systems. The predictive strength of kinetic barrier diagrams is corroborated by the fact that all the most relevant theoretical insights – from an experimental point of view – could be retrieved, even those normally requiring numerical studies to be anticipated. In this regard, an additional advantage of kinetic barrier diagrams is that it is sufficient to measure the effective rate of interconversion between states to construct them, which is often experimentally accessible. Expansion of the presented conceptual framework to more complex networks might be possible by leveraging graph theoretical techniques,[44] and diagrams might be drawn for nonequilibrium systems performing work against an external force. At present, a limitation of this conceptual framework is its application to heterogeneous systems[61] and systems comprising bimolecular reactions with two different species as reactants (A + B ⇋ C), having more than one partial conservation law.

We expect that kinetic barrier diagrams will facilitate applying nanomachine operating principles besides molecular motors. Early examples encompass driven self-assembly, related light-driven phenomena,[55,62,63] and emergent phenomena such as chemical oscillations and pattern formation.[64–66]

Supporting Information

Supporting Information is available from the Wiley Online Library or from the author. An interactive tutorial is available via the supporting information and online at this link, https://mybinder.org/v2/gl/emanuele.penocchio%2Fengspan/e4162e785e9f34502b848700c8fcfcbdf4a51595?urlpath=/tree/%2Ftutorial.ipynb.

Acknowledgements

This work was supported by the Interdisciplinary Thematic Institute ITI-CSC via the IdEx Unistra (ANR-10-IDEX-0002) within the program Investissement d'Avenir, and the European Research Council (ERC-2021-StG n. 101041933 and ERC-2015-CoG n. 681456). The authors thank Massimiliano Esposito for support, R. Dean Astumian for insightful discussions, Beatrice Bartolomei, Shuntaro Amano, and Benjamin Roberts for proofreading the manuscript, and Elisabeth Kreidt for providing the cartoons of catenane rotor.

Conflict of Interest

The authors declare no conflict of interest.

Data Availability Statement

The data that support the findings of this study are available in the supplementary material of this article.

Keywords

energy span theory, molecular machines, molecular motors, nonequilibrium systems

Received: October 8, 2022
Revised: December 11, 2022
Published online:

[1] E. Scerri, *The Periodic Table: Its Story and Its Significance*, Oxford University Press, New York, NY, USA **2019**.
[2] S. Shaik, E. Cremades, S. Alvarez, *Angew. Chem., Int. Ed.* **2019**, *58*, 13194.
[3] S. Alvarez, *Angew. Chem., Int. Ed.* **2012**, *51*, 590.
[4] R. Marcelin, *Ann. Phys.* **1915**, *9*, 120.
[5] P. Atkins, J. dePaula (Eds.), *Atkins' Physical Chemistry*, W.H. Freeman And Company, New York **2006**.
[6] W. J. Albery, J. R. Knowles, *Biochemistry* **1976**, *15*, 5631.
[7] J. J. Burbaum, R. T. Raines, W. J. Albery, J. R. Knowles, *Biochemistry* **1989**, *28*, 9293.
[8] A. Coskun, M. Banaszak, R. D. Astumian, J. F. Stoddart, B. a Grzybowski, *Chem. Soc. Rev.* **2012**, *41*, 19.
[9] G. M. Whitesides, *Angew. Chem., Int. Ed.* **2015**, *54*, 3196.
[10] B. A. Grzybowski, W. T. S. Huck, *Nat. Nanotechnol.* **2016**, *11*, 585.
[11] C. Bustamante, D. Keller, G. Oster, *Acc. Chem. Res.* **2001**, *34*, 412.
[12] R. D. Astumian, S. Mukherjee, A. Warshel, *ChemPhysChem* **2016**, *17*, 1719.
[13] A. Sorrenti, J. Leira-Iglesias, A. J. Markvoort, T. F. A. De Greef, T. M. Hermans, *Chem. Soc. Rev.* **2017**, *46*, 5476.
[14] S. A. P. Van Rossum, M. Tena-Solsona, J. H. Van Esch, R. Eelkema, J. Boekhoven, *Chem. Soc. Rev.* **2017**, *46*, 5519.
[15] M. Weißenfels, J. Gemen, R. Klajn, *Chem* **2021**, *7*, 23.
[16] K. Das, L. Gabrielli, L. J. Prins, *Angew. Chem., Int. Ed.* **2021**, *60*, 20120.
[17] Y. Feng, M. Ovalle, J. S. W. Seale, C. K. Lee, D. J. Kim, R. D. Astumian, J. F. Stoddart, *J. Am. Chem. Soc.* **2021**, *143*, 5569.
[18] D. G. Blackmond, *Angew. Chem., Int. Ed.* **2009**, *48*, 2648.
[19] E. M. Geertsema, S. J. van der Molen, M. Martens, B. L. Feringa, *Proc. Natl. Acad. Sci. USA* **2009**, *106*, 16919.
[20] R. D. Astumian, *Biophys. J.* **2015**, *108*, 291.
[21] A. Sabatino, E. Penocchio, G. Ragazzon, A. Credi, D. Frezzato, *Angew. Chem., Int. Ed.* **2019**, *58*, 14341.
[22] E. Penocchio, R. Rao, M. Esposito, *Nat. Commun.* **2019**, *10*, 3865.
[23] E. Penocchio, F. Avanzini, M. Esposito, *J. Chem. Phys.* **2022**, *157*, 034110.
[24] S. Amano, M. Esposito, E. Kreidt, D. A. Leigh, E. Penocchio, B. M. W. Roberts, *Nat. Chem.* **2022**, *14*, 530.
[25] A. Lemarchand, L. Jullien, *Phys. Chem. Chem. Phys.* **2004**, *6*, 398.
[26] S. Kassem, T. Van Leeuwen, A. S. Lubbe, M. R. Wilson, B. L. Feringa, D. A. Leigh, *Chem. Soc. Rev.* **2017**, *46*, 2592.
[27] A. I. Brown, D. A. Sivak, *Chem. Rev.* **2020**, *120*, 434.
[28] M. Baroncini, S. Silvi, A. Credi, *Chem. Rev.* **2020**, *120*, 200.
[29] C. Pezzato, C. Cheng, J. F. Stoddart, R. D. Astumian, *Chem. Soc. Rev.* **2017**, *46*, 5491.
[30] S. Borsley, E. Kreidt, D. A. Leigh, B. M. W. Roberts, *Nature* **2022**, *604*, 80.
[31] S. Borsley, D. A. Leigh, B. M. W. Roberts, *Nat. Chem.* **2022**, *14*, 728.
[32] G. J. Brouhard, L. M. Rice, *Nat. Rev. Mol. Cell Biol.* **2018**, *19*, 451.
[33] M. R. Wilson, J. Solà, A. Carlone, S. M. Goldup, N. Lebrasseur, D. A. Leigh, *Nature* **2016**, *534*, 235.
[34] R. Rao, M. Esposito, *Phys. Rev. X* **2016**, *6*, 041064.
[35] R. D. Astumian, P. B. Chock, T. Y. Tsong, H. V Westerhoff, *Phys. Rev. A* **1989**, *39*, 6416.
[36] R. D. Astumian, M. Bier, *Biophys. Chem.* **1996**, *70*, 637.
[37] G. Ragazzon, L. J. Prins, *Nat. Nanotechnol.* **2018**, *13*, 882.
[38] R. D. Astumian, *Nat. Commun.* **2019**, *10*, 3837.
[39] K. H. Ernst, A. Ludviksson, R. Zhang, J. Yoshihara, C. T. Campbell, *Phys. Rev. B* **1993**, *47*, 13782.
[40] C. Amatore, A. Jutand, *J. Organomet. Chem.* **1999**, *576*, 254.
[41] S. Kozuch, S. Shaik, *J. Am. Chem. Soc.* **2006**, *128*, 3355.
[42] C. T. Campbell, *ACS Catal.* **2017**, *7*, 2770.
[43] S. Kozuch, S. Shaik, *Acc. Chem. Res.* **2011**, *44*, 101.
[44] S. Kozuch, *ACS Catal.* **2015**, *5*, 5242.
[45] E. Solel, S. Kozuch, N. Tarannam, *Chem. Commun.* **2019**, *55*, 5306.
[46] R. Pascal, A. Pross, J. D. Sutherland, *Open Biol* **2013**, *3*, 130156.
[47] I. Derényi, R. D. Astumian, *Phys Rev E* **1999**, *59*, R6219.
[48] S. Amano, M. Esposito, E. Kreidt, D. A. Leigh, E. Penocchio, B. M. W. Roberts, *J. Am. Chem. Soc.* **2022**, *144*, 20153.
[49] M. Klok, N. Boyle, M. T. Pryce, A. Meetsma, W. R. Browne, B. L. Feringa, *J. Am. Chem. Soc.* **2008**, *130*, 10484.
[50] R. D. Astumian, *Chem. Sci.* **2017**, *8*, 840.
[51] S. Borsley, D. A. Leigh, B. M. W. Roberts, *J. Am. Chem. Soc.* **2021**, *143*, 4414.
[52] A. Albaugh, T. R. Gingrich, *Nat. Commun.* **2022**, *13*, 2204.
[53] N. Koumura, R. W. J. Zijlstra, R. a van Delden, N. Harada, B. L. Feringa, *Nature* **1999**, *401*, 152.
[54] V. Serreli, C.-F. Lee, E. R. Kay, D. a Leigh, *Nature* **2007**, *445*, 523.
[55] G. Ragazzon, M. Baroncini, S. Silvi, M. Venturi, A. Credi, *Nat. Nanotechnol.* **2015**, *10*, 70.
[56] R. D. Astumian, *Faraday Discuss.* **2016**, *195*, 583.
[57] E. Penocchio, R. Rao, M. Esposito, *J. Chem. Phys.* **2021**, *155*, 114101.
[58] S. Corra, M. T. Bakic, J. Groppi, M. Baroncini, S. Silvi, E. Penocchio, M. Esposito, A. Credi, *Nat. Nanotechnol.* **2022**, *17*, 746.
[59] S. Amano, S. D. P. Fielden, D. A. Leigh, *Nature* **2021**, *594*, 529.
[60] G. Falasco, T. Cossetto, E. Penocchio, M. Esposito, *New J Phys* **2019**, *21*, 073005.
[61] Z. Mao, C. T. Campbell, *ACS Catal.* **2019**, *9*, 9465.

[62] M. Kathan, F. Eisenreich, C. Jurissek, A. Dallmann, J. Gurke, S. Hecht, *Nat. Chem.* **2018**, *10*, 1031.
[63] R. Chen, S. Neri, L. J. Prins, *Nat. Nanotechnol.* **2020**, *15*, 868.
[64] I. R. Epstein, B. Xu, *Nat. Nanotechnol.* **2016**, *11*, 312.
[65] J. Leira-Iglesias, A. Tassoni, T. Adachi, M. Stich, T. M. Hermans, *Nat. Nanotechnol.* **2018**, *13*, 1021.
[66] S. Amano, S. Borsley, D. A. Leigh, Z. Sun, *Nat. Nanotechnol.* **2021**, *16*, 1057.